PAPER • OPEN ACCESS

Airfoil Icing Prediction with Improved Roughness Model

View the article online for updates and enhancements.

Airfoil Icing Prediction with Improved Roughness Model

Serkan Özgen and Eda Bahar Sarıbel

Middle East Technical University, Dept. Aerospace Eng., 06800, Ankara, Turkey

E-mail: `serkan.ozgen@ae.metu.edu.tr`

Abstract.
　Wind turbines are usually exposed to harsh environmental conditions, resulting in the icing of their structures. The production capability of iced wind turbines drops significantly compared to clean turbines. Understanding how ice build up is the first step in coping with its adverse effects. Analyzing the performance reduction and ice shapes on site can be challenging due to practical difficulties. Numerical analysis of iced blade sections combined with Blade Element Momentum Method can simulate the effects of exposure of wind turbines to icing weather. This paper aims to implement an improved ice accretion model for blade sections of wind turbines. The chosen analytical model is designed to compute roughness due to ice locally and employs three water state models due to icing. Roughness height characterizes the boundary layer development and alters the heat transfer coefficient distribution. The mass balance of the Extended Messinger model that is used for ice accretion prediction is improved by including the remaining water mass on the ice surface. The result of the icing simulation of NACA0012 in wet and dry regimes matches the experimental results well.

1. Introduction and Objectives

Ice accretion is a significant challenge for sustaining wind turbines' ideal performance and efficiency. Accreted ice on wind turbines leads to aerodynamic performance degradation by increasing drag and decreasing lift forces, consequently reducing power production. The effects of icing go beyond mechanical challenges. It poses economic problems due to the reduction of produced energy and potential structural damage. In wind farm sites experiencing severe icing, the loss of power production exceeds 20% of the annual energy production [1]. As the demand for clean and sustainable energy grows, understanding and mitigating the effects of icing on wind turbines become a critical constituent for developing wind energy systems.

Experimental and computational analyses are crucial steps in perceiving icing behavior and mitigating its adverse effects. Numerical analysis is a much cheaper and faster way compared to experiments. While exposing all structures of wind turbines creates a high demand on computational infrastructures, combining a 2D analysis of blade sections with BEM is a robust and sufficiently accurate way of simulation of blade performance in icing conditions. Prediction of ice accretion is a multistep simulation that includes airflow solution, droplet trajectory computation, and thermal analysis. The panel method is the first step of flow analysis of clean and iced airfoil. Implementing integral boundary layer correction allows viscous flow effects to be taken into account. Droplet trajectories are calculated starting at blade upstream and

impinge the blades. Resulting droplet collection efficiency distribution shows the distribution of water mass impinging the surface. The Extended Messinger model is used for the heat and mass balance of each panel and gives frozen water mass. In glaze ice regime, the surface covered by ice has different roughness profiles based on the water-ice fraction. First, Olsen and Walker have observed the change of roughness characteristics of ice-accreted surfaces at low temperatures [2]. The study shows that ice formation is very smooth near the stagnation point, and the rough region starts in the downstream region or out of the impingement zone. Yamaguchi and Hansman have developed a multi-zone model that determines the transition point from a smooth surface to a rough one [3]. Surface roughness fundamentally impacts heat transfer coefficient distribution and boundary layer development [4, 5]. Shin and Bond developed an empirical relation between roughness height and heat transfer coefficient based on experimental results [6]. However, the equivalent sand grain roughness defined in the correlation of Shin and Bond does not respond to the local icing variations on the surface. Also, it does not include the remaining water entrapped in accreted ice. Fortin et al. [7] introduced a local roughness model for glaze ice based on the definition of beads from Hansman and Turnock [8] and surface film from Al-Khalil et al [9].

In this paper, Fortin's analytical roughness model is implemented to an in-house code, and the results of 2D ice accretion simulation on wind turbines are presented. The effect of centrifugal force on runback water is neglected because the distance that runback water is prominently short compared to the chord of the airfoil. The intensity of ice accretion increases towards the tip of the blade. NACA0012 is chosen for this study because it is a thin airfoil similar to the tip section of the blade, and abundant experimental data is available for this airfoil geometry.

This paper aims to:

- Model the surface roughness on wind turbines due to ice accretion in wet regimes. Local roughness height changes the transition point from laminar to turbulent flow which affects the development of the boundary layer. Consequently, convective heat transfer coefficient distribution is affected.
- Model the ice shapes based on the Extended Messinger Model with improved mass and heat balance equations.
- Calculate the lift and drag forces of blade section airfoils to compare with clean geometry.

2. Methodology
Computations are accomplished using an in-house ice accretion simulation code. It is a multistep solver that handles icing problem of 2D geometries and consists of four main modules. After the geometry and ambient conditions are input, it starts solving the flowfield around the airfoil. Droplet trajectories start upstream of the blade and impinge the surface. Ice mass, runback water, and roughness are determined by mass and energy balances. This process is repeated until reaching the total exposure time.
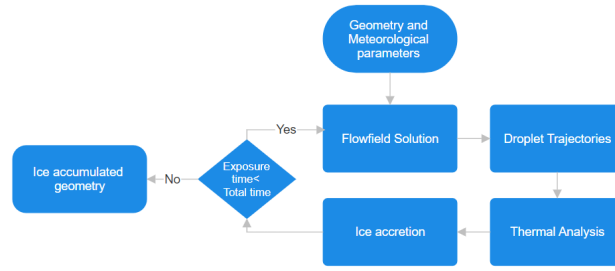
Figure 1: Flowchart of ice accretion code

2.1. Flow Field Solution

The Flow Field Solution module utilizes the Hess-Smith Panel method to determine the pressure and velocity distribution around an airfoil. This method represents the airfoil surface as a series of panels with constant singularity strengths. After determining singularity strengths, pressure values on each panel can be calculated. Lift and drag forces acting on the airfoil are found from the computed pressure distribution.

2.2. Trajectory Calculations

This module calculates the trajectories of droplets and gives the collection efficiency distribution over an airfoil employing the Lagrangian approach [10]. Each particle trajectory starts from a faraway upstream location of the leading edge. All particles are identical (monodispersed droplet size distribution) and are under drag and gravity forces only. Equations of motion for droplet trajectories are as follows:

$$m\ddot{x}_p = -D cos\gamma \tag{1}$$

$$m\ddot{y}_p = -D sin\gamma + mg \tag{2}$$

$$\gamma = tan^{-1}\frac{\dot{y}_p - V_y}{\dot{x}_p - V_x} \tag{3}$$

$$D = 1/2\rho V_{rel}^2 C_D A_p \tag{4}$$

$$V_{rel} = \sqrt{(\dot{y}_p - V_y)^2 + (\dot{x}_p - V_x)^2} \tag{5}$$

In the above equations, V_x and V_y are the components of the flow field velocity at the droplet location, and $\dot{x}_p$, $\dot{y}_p$, $\ddot{x}_p$, $\ddot{y}_p$ are the components of the droplet velocity and acceleration. γ corresponds to angle between the particle trajectory and the flow streamline. Droplet cross-sectional area and atmospheric density are denoted as A_p and ρ respectively.

Droplets are assumed to be small enough so that large droplet effects like nonsphericity, splash, and breakup of droplets are neglected. As droplets get smaller, the effects of inertia diminish proportionally. As a result, droplets diverge away from the body, and fewer particles impinge the surface.

The Droplet drag coefficient is calculated as a function of the droplet Reynolds number that is defined as $Re_d = \rho V_{rel} d_p / \mu$.

$$C_D = \frac{24}{Re_d}(1 + 0.197 Re_d^{0.63} + 2.6 \times 10^{-4} Re_d^{1.38}), Re_d \leq 3500 \tag{6}$$

$$C_D = \frac{24}{Re_d}(1.699 \times 10^{-5}) Re_d^{1.92}, Re_d > 3500 \tag{7}$$
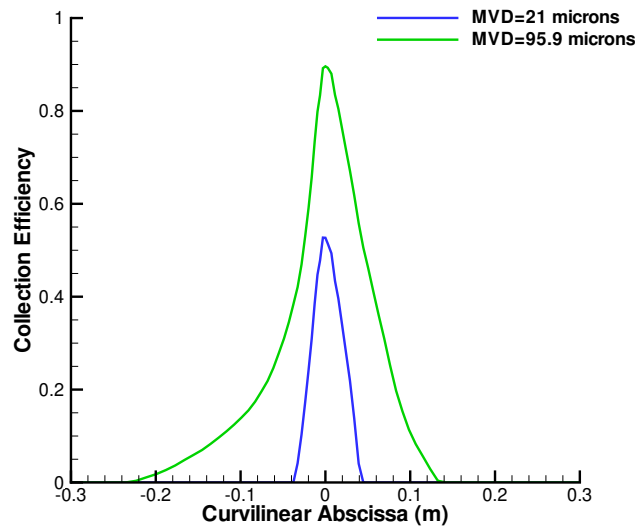

Figure 2: Droplet collection efficiency distribution around the NACA0012

Figure 2 is an example of the droplet collection efficiency distribution around the NACA0012 airfoil for two different droplet sizes. Results show that increasing droplet size increases the width of the impingement zone and the maximum collection efficiency. Both distributions show a peak near the stagnation point and a gradual decrease towards the trailing edge.

2.3. Boundary Layer Solution

The integral boundary layer method is employed to analyze and model the characteristics of the boundary layer that forms on the airfoil surface. The boundary layer starts at the stagnation point around the leading edge and begins with laminar flow characteristics. After the roughness Reynolds number reaches 600 according to Von Doenhoff criterion, flow characteristics change into turbulent. The transition from laminar to turbulent flow affects skin friction, heat transfer, and momentum thickness development. Altering the original airfoil body by adding the boundary layer displacement thickness allows viscous effects to be accounted for in the subsequent panel method solutions [12].

In a laminar region, the heat transfer coefficient is defined as [13]:

$$h_c = \frac{0.296 k U_e^{1.437}}{\sqrt{\nu \int_0^s U_e^{1.87} ds}} \tag{8}$$

where s is the streamwise distance along the airfoil surface starting at the stagnation point and the dynamic viscosity of air is denoted as k and $\nu = \mu/\rho$. The thermal conductivity of air, k

is calculated by using viscosity computed from Sutherland's viscosity law with the assumptions of constant Prandtl number and specific heat. Note that the heat transfer coefficient of laminar flow does not depend on roughness.

Thwaites' formulation is used to calculate laminar momentum thickness calculation [12]:

$$\frac{\theta_l^2}{\nu} = \frac{0.45}{U_e^6} \int_0^s U_e^5 ds \tag{9}$$

The convective heat transfer coefficient of turbulent flow is a function of roughness height and is implemented from Kays and Crawford [13]:

$$h_c = St\rho U_e C_p \tag{10}$$

where C_p is the specific heat of air. The Stanton number, St is defined as [13]:

$$St = \frac{C_f/2}{Pr_t + \sqrt{(C_f/2)/St_k}} \tag{11}$$

where the turbulent Prandtl number, Pr_t is taken as 0.9 and the roughness Stanton number is found from [13]:

$$St_k = 1.92Re_k^{-0.45}Pr^{-0.8} \tag{12}$$

where $Re_{k^*} = \rho u_* k_s/\mu$ is the boundary Reynolds number and $Pr = \mu C_p/k$ is the laminar Prandtl number. u_* is the friction velocity, given by:

$$u_* = U_e\sqrt{C_f/2} \tag{13}$$

The Makkonen relation is employed for the skin friction coefficient C_f [13]:

$$\frac{C_f}{2} = \frac{0.1681}{[ln(864\theta_t/k_s + 2.568)]^2} \tag{14}$$

Turbulent momentum thickness θ_t is defined by [13]:

$$\theta_t = \frac{0.036\nu^{0.2}}{U_e^{3.29}} \left(\int_{s_{tr}}^s U_e^{3.86} ds \right)^{0.8} + \theta_{tr} \tag{15}$$

where θ_{tr} is the laminar momentum thickness at the transition location and is found from equation (9).

2.4. Ice Accretion and Roughness Model

The Extended Messinger Model is a mathematical model used to simulate and predict the formation of ice accretion on surfaces based on phase change or the Stefan problem. The model is an extension of the original Messinger model and provides a more comprehensive representation of the ice accretion process. Ice and water layers constitute the control volume. The solution to Stefan's Problem is directed by continuity equation, energy equations for ice and water layers, and phase change at ice/water interface [14].

$$\frac{\partial T}{\partial t} = \frac{k_i}{\rho_i C_{pi}} \frac{\partial^2 T}{\partial y^2} \tag{16}$$

$$\frac{\partial \theta}{\partial t} = \frac{k_w}{\rho_w C_{pw}} \frac{\partial^2 \theta}{\partial y^2} \tag{17}$$

$$\rho_i \frac{\partial B}{\partial t} + \rho_w \frac{\partial h}{\partial t} = \rho_a \beta V_\infty + \dot{m_{in}} - \dot{m_{e,s}} \tag{18}$$

$$\rho_i L_f \frac{\partial B}{\partial t} = k_i \frac{\partial T}{\partial y} + k_w \frac{\partial \theta}{\partial y} \tag{19}$$

In the above equations, the temperatures are denoted by θ and T, thermal conductivities denoted by k_w and k_i for water and ice layers respectively. C_{pw} and C_{pi} are the specific heats and h and B are the thicknesses of water and ice layers respectively. The left side of the equation (18) shows impinging, runback, and evaporating mass flow rate for control volume respectively. The liquid water content and latent heat solidification are denoted by ρ_a and L_F in eq.(19).

Ice surface roughness is determined by water state model [7]. Rime ice freezes upon contact with cold surfaces. It has a rough and granular surface texture due to frozen water beads and trapped air between them. Although its surface is rougher compared to glaze ice, it disrupts the flow to a lesser extent. The roughness of rime ice is determined by maximum bead height before incoming water droplets fill the gaps between beads.

$$k_s = e_b \tag{20}$$

Bead height is found from the balance of forces acting on the beads. Aerodynamic force, gravitational force, and surface tension influence the stability of the bead. Maximum bead height represents the stationary bead height before the equilibrium of these forces is broken. Calculation of bead height is done according to the direction of forces;

$$e_b = \frac{\pm \left(R_W - \sqrt{R_W^2 \pm 4R_g \Delta\theta_c} \right)}{2R_g} \tag{21}$$

At higher temperatures droplets can not solidify entirely, and a water layer regime develops on top of the ice. Behavior of the water layer is modeled in three regimes: film, bead, and rivulet. The film regime develops near the stagnation region. The remaining water covers the surface after excessive water runs back towards the trailing edge. Roughness and height of film regime are calculated from [15]:

$$k_s = 0.75\tau_w/\mu_w \cdot \sqrt{e_f^3/g} \tag{22}$$

where τ_w and μ_w are the wall shear stress and water dynamic viscosity. The film height e_f is given by [7]:

$$e_f = \sqrt{\frac{2}{\tau_w}} \sqrt{\frac{\mu_w m_w}{\rho_w \Delta b \Delta t}} C_{cal} \tag{23}$$

where m_w and ρ_w are the liquid water mass and its density. The width of control volume width and time step are denoted by Δb and Δt.

Remaining water mass, m_{rmw} entrapped in the control volume is calculated from [7]:

$$m_{rmw} = \rho_w A_p e_{f,min} \tag{24}$$

where A_p is the control volume surface and $e_{f,min}$ is the minimum film height.

If the water height is less than the minimum film height $e_{f,min}$, impinging water forms beads. In a dry regime, droplets freeze instantly and accumulate on top of each other. At higher temperatures, water beads may not solidify completely. Liquid water mass runs back and fills the gap between partially frozen beads. The surface roughness of the bead regime is equal to the thickness of the ice until the ice thickness reaches the maximum bead height. The surface roughness is constant after that.

On the upper surface, excessive water may run out of the impingement zone and freeze there. This is called the rivulet regime due to its similar look. The roughness and height of the rivulet are the same and equal to the maximum bead height. Residual water is the unfrozen water within the control volume.

$$k_s = e_r = e_b \tag{25}$$

$$m_{rmw} = \rho_w A_p e_f (1 - f) \tag{26}$$

where f represents the solid fraction of the water mass. In runback, water sheds on a lower surface due to gravity.

3. Results and Discussion

The developed in-house code produces results for comprehensive icing analysis of the NACA0012 airfoil. The obtained results are compared with the experimental data. Meteorological conditions are listed in Table 3. The ambient temperatures studied represent rime ice and mixed glaze/rime ice conditions. The airfoil is exposed to icing conditions for 360 seconds. The 30-second time-step has been found to be the optimum interval for accuracy and computational time.

Condition	Value
Accretion time	360s
Chord	0.5334m
Angle of attack	4°
Air speed	67.05 m/s
Liquid water content	$1g/m^3$
Median volumetric diameter	$20\ \mu$
Ambient Temperature	-4.4, -28.3 ^oC
Atmospheric pressure	101300 Pa

Experimental results are those reported by Shin and Bond [6]. The experiment was performed with the blade attached vertically in the NASA Lewis Icing Research Tunnel (IRT). Therefore, in the experiments, the gravity force is parallel to the airfoil plane and its effect is small compared to aerodynamic forces. Also, computational results of the CIRA computational tool are compared with predicted ice shapes [16].
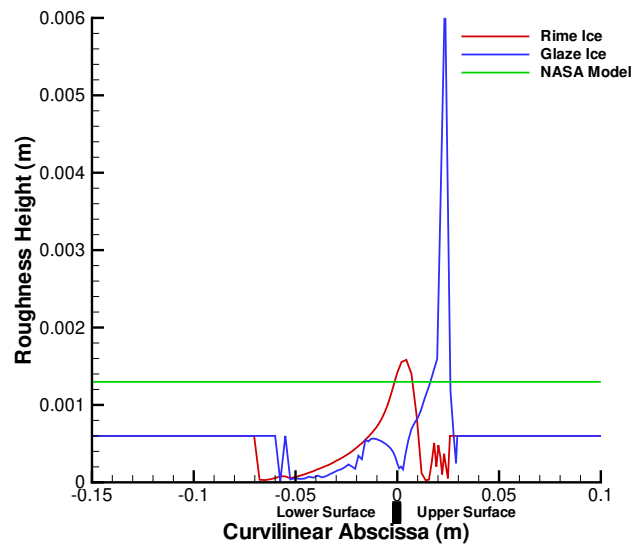
Figure 3: Roughness distribution of the last step of ice accretion

Figure 3 shows the surface roughness of iced geometry. The blue line represents the roughness distribution of -4.4^oC obtained at the final computational step. Water film is assumed to be aerodynamically smooth. The peak point of glaze ice roughness corresponds to the horn shape seen in Figure 4. Flow separation after passing the horn causes a sudden drop in roughness height. It can be noted that the flowfield solution does not capture this phenomenon. Droplets are expected to accumulate in the separation region. Flow can accumulate particles in the separation zone. The shape difference on the upper surface between the experiment and predicted ice shapes in Figure 4 may be an indication of this. NASA roughness model [17] gives roughness height as 1.298 mm for glaze ice and is also shown in Figure 3 . It can be seen that this correlation does not reflect local geometry and ice characteristics and water layer state.
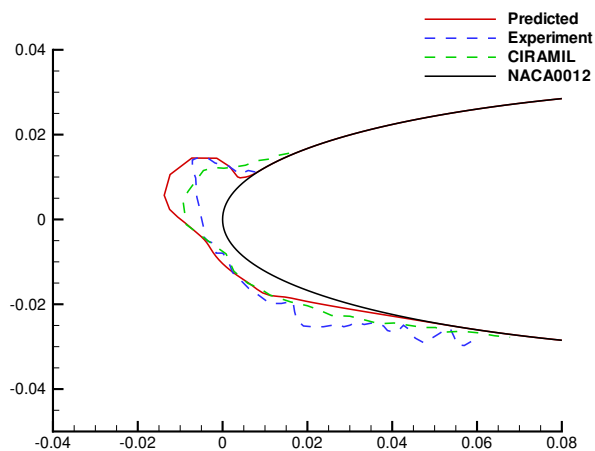

Figure 4: Ice accumulation at -4.4^oC

It can be seen in Figure 4 that the size, location, and angle of the horn on the upper surface are predicted fairly accurately. However, the size of the horn is slightly overpredicted, which may be due to the runback water model used. In the current model, it is assumed that all excess water passes to the next neighboring downstream control volume (panel). Although the water state is modeled in the current model, water film movement is not modeled. This may be part of future endeavors.

The impingement zone of the lower surface is narrower compared to the experiment. Wavy ice accumulation through the edge may be evidence of runback water and rivulet ice. The improved roughness model states that all water mass in the lower surface is shed. This statement may not reflect reality due to the force of adhesion. The surface material has a significant effect on the shedding of water. As mentioned above, water film movement can be modeled as well.
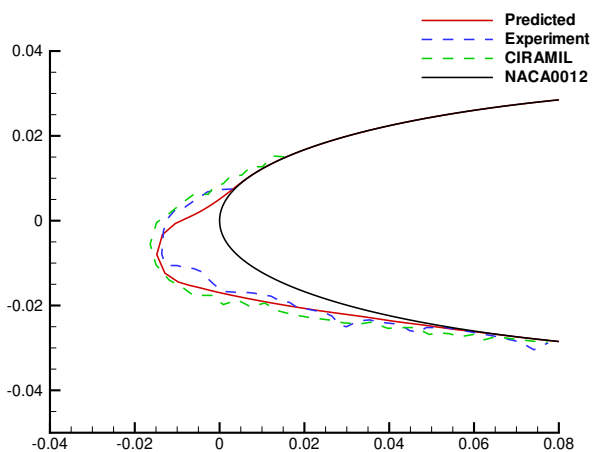

Figure 5: Ice accumulation at $-28.3^{o}C$

The roughness distribution of rime ice in figure 3 has a similar behavior to the collection efficiency distribution. It reaches the peak value at the stagnation point and has a smooth distribution. Although rime ice is much rougher than the glaze ice near the leading edge, the final glaze ice shape shown in Figure 4 is more detrimental to aerodynamic performance than the rime ice. This is due to the fact that at regions other than the stagnation regions, glaze ice shape produces much more severe roughness levels and ice thicknesses compared to rime ice. It can be seen from Figure 5, rime ice follows the contours of the geometry and it is like an extension of the leading edge of the airfoil.

There is good agreement between experiment and predicted ice shape results in Figure 5. The impingement limits hence extent of ice on the upper surface are very similar. It has to be mentioned that monodispersed cloud droplet size distribution is considered in this study, while a droplet size distribution spanning smaller and larger droplets is more realistic. A droplet size distribution like the Langmuir-D distribution may be used in order to improve the accuracy of the results [11].

4. Conclusion

Ice shape and surface roughness predictions are performed over NACA0012 using the improved roughness model that includes local surface roughness and remaining water masses. The

analytical model results have been compared with experimental data and numerical results of other methods in the literature.

Glaze ice results show that the improved roughness model can accurately predict the angle, size, and location of the horn on the upper surface. Overprediction on the other side may be the result of the runback water model. The local roughness heights of the glaze ice result has an expected distribution based on water layer regimes. The roughness peak location matches the horn location. In the dry regime, the predicted ice shape result is fairly similar to the experimental result. The developed in-house tool is slightly more accurate compared to the other model. The roughness distribution of rime ice is parallel to the droplet collection efficiency.

The accuracy of the results may be improved by implementing a droplet size distribution. Also, the modeling of water film movement can be studied in the future.

References

[1] Wallenius, T., and Lehtomäki, V. (2015). Overview of cold climate wind energy: Challenges, solutions, and future needs. WIREs Energy and Environment, 5(2), 128–135. https://doi.org/10.1002/wene.170

[2] Olsen, W., and Walker, E. Experimental Evidence for Modifying the Current Physical Model for Ice Accretion on Aircraft Surfaces, NASA Technical Memorandum 87184 , May, 1986

[3] Yamaguchi, K., Hansman, JR., R., and Kazmierczak, M. (1991). Deterministic multi-zone ice accretion modeling. 29th Aerospace Sciences Meeting. https://doi.org/10.2514/6.1991-265

[4] Bragg, M., Kerho, M., and Cummings, M. (1995). Airfoil boundary layer due to large leading-edge roughness. 33rd Aerospace Sciences Meeting and Exhibit. https://doi.org/10.2514/6.1995-536

[5] Bragg, M., Cummings, M., and Henze, C. (1996). Boundary-layer and heat-transfer measurements on an airfoil with simulated ice roughness. 34th Aerospace Sciences Meeting and Exhibit. https://doi.org/10.2514/6.1996-866

[6] Shin J. and Bond T., Experimental and Computational Ice Shapes and Resulting Drag Increase for a NACA 0012 Airfoil, NASA Technical Manual 105743, January, 1992.

[7] Fortin, G., Ilinca, A., Laforte, J.-L., and Brandi, V. (2004). New roughness computation method and geometric accretion model for airfoil icing. Journal of Aircraft, 41(1), 119–127. https://doi.org/10.2514/1.173

[8] Hansman, R. J., and Turnock, S. R. (1989). Investigation of surface water behavior during Glaze Ice Accretion. Journal of Aircraft, 26(2), 140–147. https://doi.org/10.2514/3.45735

[9] Al-Khalil, K. M., Keith, JR., T. G., and De Witt, K. J. (1991). Further development of an anti-icing runback model. 29th Aerospace Sciences Meeting. https://doi.org/10.2514/6.1991-266

[10] Özgen, S., Canıbek, M., Ice accretion simulation on multi-element airfoils using extended Messinger model, Heat and Mass Transfer, Vol. 45, 305-322, 2009.

[11] Wright, W.B. and Potapczuk, M.G. 2004 Semi-empirical Modeling of Icing Physics, NASA/TM-2004-212916.

[12] Schlichting, H., Boundary-Layer Theory, 7th Ed., McGraw-Hill, 1979.

[13] Gent, R. W., Dart, N. P., and Cansdale, J. T. (2000). Aircraft icing. Philosophical Transactions of the Royal Society of London. Series A: Mathematical, Physical and Engineering Sciences, 358(1776), 2873–2911. https://doi.org/10.1098/rsta.2000.0689

[14] Myers TG (2001) Extension to the Messinger model for aircraft icing. AIAA J 39(2):211–218

[15] Al-Khalil, K. M., Keith, T. G., DeWitt, K. J., Nathman, J. K., and Dietrich, D. A. (1990). Thermal analysis of engine inlet anti-icing systems. Journal of Propulsion and Power, 6(5), 628–634. https://doi.org/10.2514/3.23264

[16] Fortin, G., Laforte, J.-L., and Ilinca, A. (2006). Heat and mass transfer during ice accretion on aircraft wings with an improved roughness model. International Journal of Thermal Sciences, 45(6), 595–606. https://doi.org/10.1016/j.ijthermalsci.2005.07.006

[17] Wright, W.B., Gent, R.W. and Guffond, D. (1997). DRA/NASA/ONERA Collabration on Icing Research, Part II. Prediction of Airfoil Ice Accretion, NASA CR-202349.